REVIEW AND RECENT DEVELOPMENT IN COMBINING PHOTOLUMINESCENCE- AND ELECTROLUMINESCENCE-IMAGING WITH CARRIER LIFETIME MEASUREMENTS VIA MODULATED PHOTOLUMINESCENCE AT VARIABLE TEMPERATURES

H. Höffler[1], F. Schindler[1], A. Brand[1], D. Herrmann[1], R. Eberle[1], R. Post[3], A. Kessel[2], J. Greulich[1], M.C. Schubert[1]
[1]Fraunhofer Institute for Solar Energy Systems ISE, Heidenhofstrasse 2, 79110 Freiburg, Germany
[2]Intego GmbH, Henri-Dunant-Str. 8, 91058 Erlangen, Germany
[3]University of Freiburg, Friedrichstr. 39, 79098 Freiburg, Germany

ABSTRACT: In this contribution we give a review on measurement techniques which allow to measure the minority carrier lifetime in silicon solar cell precursors in a spatially resolved manner. The measurement of spatially resolved lifetime using the combination of modulated photoluminescence and photoluminescence imaging (Mod-PL calibrated PLI) is reviewed in detail. Based on our experience we present a canon of recommendations for the features of the experimental setup and the data analysis methods, which we consider to be necessary for Mod-PL calibrated PLI measurements. Using these recommendations the results of selected samples are checked for reproducibility, self-consistency and cross compared to photoconductance based results. Reproducibility is observed to be better than 1 %. The dependence on critical input parameters like measurement frequency and calibration position is observed to be smaller than 5 %. Comparison to photoconductance decay measurements for a broad variety of specimen throughout our R&D environment reveals deviation of less than 10 % for most samples, which can partly be attributed to potential artifacts in the photoconductance measurements. An overview on some selected applications of temperature controlled Mod-PL calibrated PLI measurements in an R&D environment is given. The overview includes the applications: prediction of efficiency potential of silicon material, process optimization of laser processes, quantitative determination of metal induced recombination, quantitative determination of series resistance, determination of material specific temperature coefficients and classification and localization of material defects via temperature and injection dependent lifetime spectroscopy.

Keywords: c-Si; Characterization; Photoluminescence; Lifetime; Silicon

1 INTRODUCTION AND REVIEW

This contribution gives an overview on the potential arising from temperature controlled spatially resolved minority carrier lifetime measurements on silicon wafers. In literature there is a great variety of different methods, which can be used to obtain spatially resolved lifetime. In the past years we have developed a measurement setup and an evaluation software (modulum) with the aim of combining those methods, which we consider to be a robust canon in order to obtain spatially resolved lifetimes and other detailed information on silicon wafers and solar cells. After a brief review of the existing methods for lifetime and spatially resolved parameter measurements in section 1, we treat the evaluation methods and the key aspects of the experimental setup, which are combined in modulum in detail in section 2. Experimental results, which support the reliability of the measurement method by consistency checks and cross comparison to other lifetime measurement techniques are shown in section 3. In section 4 we show application examples on various topics from our research and development environment. The recent development in detailed characterization using temperature dependent spatially resolved lifetime measurements, which is enabled by the temperature controlled stage of the measurement setup, is sketched in section 5.

1.1 Review on lifetime measurement

The injection dependent minority carrier lifetime is an important characterization parameter for semiconductors since their very discovery [1, 2] and lifetime measurements on silicon experienced a renaissance in the 90s [3]. In the photovoltaic (PV) community lifetime measurements are used for process control in different manufacturing states of silicon solar cells for more than 20 years [4]. There are various approaches to measure the

carrier lifetime. An overview is given in [5] (section 7.4, 7.5). The most common approach in the PV community is probably the monitoring of photoconductance decay [6] via an rf-bridge, which is often combined with measuring the generation rate and calculating the lifetime via the continuity equation in its steady-state [7] or in its generalized [8] form. Photoconductivity is alternatively often monitored by microwave reflectance [9, 10]. The time resolved monitoring of the photoluminescence (PL) signal is another approach to determine the carrier lifetime in semiconductors [11, 12]. For silicon there are different evaluation approaches, which lead from the time resolved PL signal to carrier lifetime. Square-wave-shaped excitation has been used in [13, 14]. Giesecke *et al.* [15] proposed an analysis of the time shift between excitation and PL signal allowing a lifetime determination without a priori knowledge of substrate doping. The probably most established approach is the self-consistent calibration of PL lifetime measurements, which was introduced by Trupke *et al.* [16] in 2005. This approach and some conceptual advances [17] (section 8.2.3) will be reviewed in detail in section 2. This lifetime measurement approach will be called modulated-PL (Mod-PL) in following.

1.2 Review of spatially resolved lifetime measurements

Spatially resolved lifetime measurements can coarsely be categorized into scanning and imaging techniques. Scanning techniques have been used from early on [18]. Examples are light beam induced current [19] or microwave detected photoconductivity (MDP) [20]. Scanning techniques usually directly reveal the lifetime at a certain position and hence do not need further calibration. Nevertheless they may often be rather slow, of little resolution or suffer from severe defects caused by carrier diffusion. With the evolution of infrared cameras imaging techniques became more frequent. Before the

advent of PL-imaging (PLI) [21], carrier density imaging (CDI) [22, 23] was conducted using free carrier absorption (FCA). Imaging techniques by themselves usually just reveal grayscale images in arbitrary units, which correlate to the local lifetime in a certain manner. In order to calibrate these images to lifetime, they have to be combined with a lifetime measurement technique at a certain position in the correct manner. This is in principle possible with any lifetime measurement technique. A commonly used procedure is the calibration of PL images with lifetime measurements via photoconductance [24], which has been improved in [14, 17] by taking the sensitivity of the rf-coil into account. The combination of PLI [21] and Mod-PL [16, 17] was proposed by Giesecke *et al.* in [25]. The key feature of this contribution is the correct averaging procedure. The combination of PLI and Mod-PL is discussed in detail in section 2.

1.3 Review of electroluminescence based techniques

If the excitation of charge carriers during luminescence imaging is caused by an externally applied voltage one speaks of electroluminescence imaging (ELI) [26] rather than PLI. ELI can only be applied to finished solar cells. In EL images resistance effects can be made visible. The combination of ELI and PLI allows the determination of the spatially resolved series resistance in a quantitative way by different methods [27–30]. Glatthaar *et al.* recommended a method called 'coupled determination of series resistance and dark saturation current density' (C-DCR) [31]. The method has been evaluated more closely in [32–35] and is reviewed in detail in section 2.5. It is also possible to measure the lifetime if the charge carrier excitation by the external voltage is modulated in time. One speaks of dynamic electroluminescence [36].

2 DEFAULT CANON OF MEASUREMENT METHODS AND EXPERIMENTAL SETUP

This section explains the default measurement procedure and the evaluation models, which have been implemented to the above mentioned measurement setup (modulum) that was developed over the past years.

2.1 Theory of modulated photoluminescence (Mod-PL)

During a Mod-PL lifetime measurement [16] a silicon wafer is homogeneously illuminated by a homogenized continuous wave (cw) laser with a wavelength of around 800 nm. The illumination intensity is modulated with a selectable frequency. The selection of the optimal frequency depends on the sample under investigation. An automatic detection procedure of the optimal frequency is part of the evaluation software. The generation rate $G(t)$ and the PL signal of the sample $\phi(t)$ are measured over time for a number of cycles during the overall integration time. Figure 5 shows an example of the measured data recorded at a frequency of 22 Hz. It should be noted that $G(t)$ needs to be measured in absolute units, while it suffices to measure $\phi(t)$ in arbitrary units. In order to determine $G(t)$ the photon flux impinging on the sample $j_\gamma(t)$ is measured by the experimental setup and the generation rate is determined via:

$$G(t) = \frac{j_\gamma(1 - R)}{W} \quad (1)$$

where R is the front reflectance and W is the thickness of the sample. The determination of the injection dependent lifetime is based on equation (2) and (3), which follow from the continuity equation and the fact that the radiative recombination rate is proportional to the product of the electron and hole densities [37].

$$\Delta n(t) = \frac{-a \cdot N_{dop} + \sqrt{a^2 \cdot N_{dop}^2 + 4a \cdot \phi(t)}}{2a} \quad (2)$$

$$\tau\big(\Delta n(t)\big) = \frac{\Delta n(t)}{G(t) - \frac{\partial \Delta n(t)}{\partial t}} \quad (3)$$

Equation (2) relates the excess carrier density Δn to the PL signal $\phi(t)$ via the sample doping N_{dop} and a calibration factor a. Equation (3) relates the lifetime τ to the excess carrier density via the generation rate. The knowledge of the calibration factor would hence allow the determination of the injection dependent lifetime directly from the measured PL signal. Unfortunately the factor a depends on the experimental setup and additionally on the optical properties of the sample in a complicated way [38]. The key idea of the self-consistent calibration approach is that the measured data is decomposed into an increasing part $G_{up}(t)$, $\phi_{up}(t)$ and a decreasing part $G_{down}(t)$, $\phi_{down}(t)$. For reasons of consistency both parts need to lead to the same result. They need to be free of hysteresis. The calibration factor a is now determined by guessing it iteratively until the difference between the increasing and the decreasing part is minimized. The calibration factor a contains the coefficient of radiative recombination B. It was shown in [39] that B depends on the excess carrier density itself. Since the dependence is known the calibration factor a is parameterized according to [17] (appendix A.5). This way the evaluation procedure takes the dependence $a(\Delta n)$ into account. Figure 6 shows an example of the injection dependent lifetime evaluated by this procedure.

2.2 Luminescence imaging (PLI)

Steady state luminescence imaging [21, 26] makes use of the fact that the spatially resolved luminescence signal φ_{xy} detected by a camera is proportional to the local product of electron density n and hole density p while the sample is illuminated with an irradiation causing a constant generation rate G_0:

$$\varphi_{xy} = A \cdot n_{xy}p_{xy} = A \cdot \Delta n_{xy}(\Delta n_{xy} + N_{dop}) \quad (4)$$

Here A is a calibration factor depending on the setup and the sample properties. Note that this is different to the previously mentioned factor a, because two different signals respectively detectors are addressed. Assuming the steady-state condition and no lateral currents within the sample the generation rate G_0 and the recombination rate R can be assumed to be equal and Δn can be expressed through a local lifetime τ_{xy} via $\Delta n_{xy} = G_0\tau_{xy}$. It hence follows that the local luminescence intensity is connected to the local lifetime via:

$$\varphi_{xy} = A \cdot G_0\tau_{xy}(G_0\tau_{xy} + N_{dop}) \quad (5)$$

It should be noted that the absence of lateral current is not always strictly given as discussed in [40]. Nevertheless this is negligible for most relevant cases. The knowledge of the calibration factor A would give direct access to the spatially resolved lifetime. It´s determination procedure is described in the following.

2.3 Spatially resolved lifetime

The method, which measures the spatially resolved lifetime combining PLI and Mod-PL will be called 'Mod-

PL calibrated PLI' in the following. The injection dependent lifetime $\tau(\Delta n)$ measured by Mod-PL can equally be interpreted as generation dependent lifetime $\tau(G)$. The constant illumination of the sample during the PLI measurement gives rise to a constant generation rate G_0. The lifetime evaluated at this very generation rate shall be called $\tau_{QSSL} = \tau(G)|_{G=G_0}$. The Mod-PL detector has a certain field of view relative to the camera used for the PLI measurement. The field of view from one of our laboratory setups is illustrated in Figure 1. It can be quantified by a sensitivity function S_{xy}, which fulfills $\sum_{xy} S_{xy} = 1$. The key idea of Mod-PL calibrated PLI is to apply the correct relation between τ_{QSSL} an the local lifetimes τ_{xy}. As shown and derived in [25] it is *not* correct that τ_{QSSL} is a sensitivity weighted arithmetic mean of the local lifetimes as one might intuitively expect. It is rather related to the local lifetimes via an intensity weighted mean according to:

$$\tau_{QSSL} = \frac{\sum_i\left(S_{xy}\tau_{eff,xy}{}^2\right)}{\sum_i\left(S_{xy}\tau_{eff,xy}\right)} \tag{6}$$

This can qualitatively be understood by considering that high lifetime regions emit more luminescence light and hence contribute more strongly to the signal $\phi(t)$ detected by the Mod-PL detector. Combining equation (5) and equation (6) will result in an equation where the calibration factor A is the only unknown, which has to be solved numerically. The knowledge of A then directly allows to calculate the spatially resolved lifetime and the spatially resolved excess carrier density at the given generation rate G_0 from equation (4) and (5). It should be noted that the factor A is not strictly independent from position, because (same as the other calibration factor a) it depends on the excess carrier density itself. Again this is taken into account by an iterative evaluation procedure.

If the local excess carrier density Δn_{xy} is known it is straightforward to calculate the local implied voltage $iV_{oc,xy}$ according to:

$$iV_{oc,xy} = V_t \ln\left(\frac{\Delta n_{xy} \cdot \left(\Delta n_{xy} + N_{dop}\right)}{n_{i,xy}{}^2}\right) \tag{7}$$

Here V_t is the temperature voltage and n_i the intrinsic carrier density. The intrinsic carrier density is considered to be position dependent in equation (7), because doping- and injection-dependent band gap narrowing is taken into account according to Schenk [41].

In some cases it can be useful to represent the iV_{oc} image in terms of dark saturation current density $j_{0,xy}$. Again this is straight forward. If a one diode behavior is assumed $j_{0,xy}$ calculates via:

$$j_{0,xy} = j_{gen} \cdot e^{-iV_{oc,xy}/V_t} \tag{8}$$

where the generation current j_{gen} is calculated from the measured generation rate.

2.4 Lifetime imaging at different illumination levels

A series of lifetime images of one wafer at different illumination levels is the experimental input, which is needed for an efficiency limiting bulk recombination analysis (ELBA) [42, 43]. A series of voltage images (often referred to as Suns-PLI [44, 45]) is needed for a determination of the local pseudo fill factor.

There are two ways this series can be obtained. In both cases a series of N PL-images at different generation rates $G_{0,i}$ (i running from 1 to N) is needed. Intuitively one might now apply Mod-PL calibrated PLI to each of these images separately. That is determining N calibration factors A_i by using N different lifetimes $\tau_{QSSL,i}$. The different calibration factors A_i obtained by this procedure should be equal within the measurement uncertainty. Nevertheless it shows that the uncertainty of τ_{QSSL} becomes large for low generation rates. It is hence recommended and implemented as the default procedure to our evaluation software that one obtains only a single calibration factor at a rather high illumination level (an illumination of 1 sun[1] might serve as a rule of thumb). Intuitively one might directly insert this calibration factor to equation (4), (5) and (7) to calculate the desired images. Nevertheless the dependence of the calibration factor to excess carrier density has to be taken into account here as well, which is done by the evaluation software of modulum using the parameterization of [17] (appendix A.5).

2.5 Electroluminescence imaging and series resistance

An external contacting frame connected to a source-sink allows combining ELI and PLI and the determination of local series resistance $R_{S,xy}$ and dark saturation current density $j_{0,xy}$ via C-DCR [31]. Four images at different working points along the *IV*-curve are recorded. One at low illumination and open circuit $\varphi_{low,oc,xy}$ (0.2 suns) is used to determine a factor C_{xy} via:

$$C_{xy} = \varphi_{low,oc,xy} \cdot e^{-V_{term}/V_t} \tag{9}$$

Here V_{term} is the terminal voltage measured by the source-sink. Two other images at high illumination (1 sun) and two different working points $\varphi_{high,25,xy}$ and $\varphi_{high,75,xy}$ are recorded. A forth image is recorded at high illumination and short circuit $\varphi_{high,jsc,xy}$. In order to take diffusion limited carriers into account the image at short circuit is subtracted from the images at the working points leaving two 'net-images' $\varphi_{net,25,xy}$ and $\varphi_{net,75,xy}$. These 'net-images' are calibrated to voltage using the previously obtained factor C_{xy}, which then results in two voltage images $V_{25,xy}$ and $V_{75,xy}$. Now a system of two equations follows directly from Ohm´s law and a terminal connected diode assumption:

$$R_{xy} = \frac{V_{term,i} - V_{25,i}}{j_{0,xy}e^{V_{i,xy}/V_t} - j_{sc}} \tag{10}$$

Here the index i runs through the two working points 25 and 75 and the terminal voltages and j_{sc} is measured by the source-sink. The system of two equations can be solved with respect to their two unknowns R_{xy} and $j_{0,xy}$. The solution is written down in [46] (section 7.1) and implemented into the evaluation software modulum.

2.6 Key aspects of the experimental setup

While a typical PL-EL imaging setup is described in [47] (apart from numerous variations, which are commercially available) and the evolution of a setup used for Mod-PL lifetime measurements is described in [17] (chapter 7), we will give a brief overview on the key hardware aspects of the combined setup (modulum) here.

---

[1] 1 sun is defined as a photon flux of $2.5 \cdot 10^{17}$ photons/($cm^2 \cdot$ s) impinging on the sample.

PL imaging: The photoexcitation is realized by fiber-coupled 808 nm diode laser. The fiber is coupled into a beam shaper which homogeneously illuminates an area of 180 x 180 mm² with a deviation of less than 10% throughout the area. A short pass filter is placed behind the beam shaper in order to avoid light of larger wavelength to escape from the beam shaper. The impinging photon flux is measured by a diode, which is initially calibrated by a WPVS reference cell calibrated by Fraunhofer ISE CalLab. The wafers are placed on a chuck of non-luminescent material. Special care is taken to avoid any luminescent material within the whole measurement chamber. The luminescence emitted from the wafer is detected by a silicon CCD camera positioned above the chuck. A stack of filters is positioned in front of the camera in order to make sure that only light between 950 nm and 1000 nm is detected.

Mod-PL: The modulated photoexcitation is realized by the same laser/beam shaper unit as in PLI. The luminescence signal is detected by a detection unit which consists of a photosensitive diode, a filter stack similar to the one in front of the camera and an infrared lens. The optics of the detection unit leads to a field of view, which is visualized in Figure 1.

Chuck and temperature control: For standard measurements the chuck is kept at 25°C which is realized by temperature controlled water running through a cooling block below the chuck, which is thermally connected to the chuck's surface. A very recent feature of the setup is its ability to control temperature between 15°C and 200°C. Up to 80°C this is realized by Peltier elements placed between the cooling block and the chuck surface. Above 80°C this is realized by electrical heating elements directly under the chuck surface. Peltier and heating elements are controlled by a pulse width modulation (PWM) unit. The temperature measurement is realized by a Pt-100 element placed directly underneath the chuck's surface.
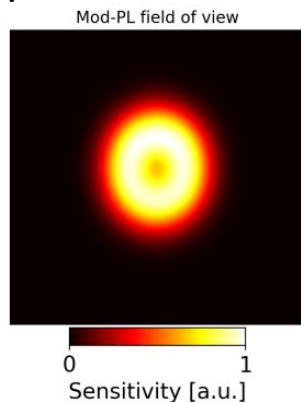

Figure 1: Field of view of the Mod-PL detector measured on one of our laboratory setups with an area of 160 x 160 mm²
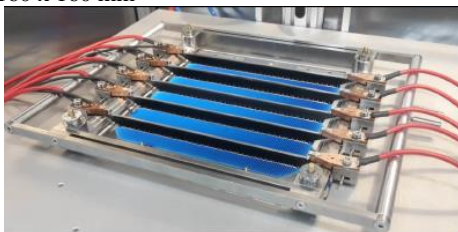

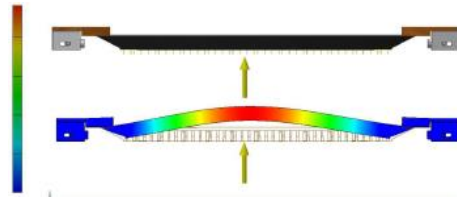Figure 2: Photo of the contacting unit

Figure 3: Sketch of the bending simulation (taken from [48]).

Contacting unit: A special contacting unit for ELI has been designed, which enables contacting cells with 3 to 6 busbars. A photograph is shown in Figure 2. The special design focused on three aspects. Firstly the height of the contacting bars was kept as low as possible in order to avoid shadowing originating from the camera perspective. Secondly the brass contacting bars were coated and covered with non-luminescent material. Thirdly the impact of external contacting errors [33] was reduced as far as possible. This was done by increasing the number of load pins on the one hand. On the other hand simulations on the bending induced by the force of the contacting pins were performed (see Figure 3). The contacting bars were then constructed with an intentional convex bow in order to compensate the bending. Details on the design can be found in [48].

3 EXPERIMENTAL RESULTS AND VALIDATION APPROACHES

In this section the results of an experiment are shown, in order to validate the Mod-PL calibrated PLI measurement procedure. Lifetime results are cross compared to results obtained by QSSPC measurements and the consistency of the Mod-PL calibrated PLI method is investigated.

3.1 Design of experiment

10 silicon wafers in different processing states are chosen from our R&D environment. The wafers are chosen in order to represent a broad range of possible specimen. They feature different materials, different surface morphologies, differently passivated or doped surfaces, different wafer formats (including one intentionally broken wafer) and different overall lifetime regimes. Wafers 9 and 10 are metallized at the rear side. The PL images of the wafers scaled in arbitrary units are shown in Figure 4.
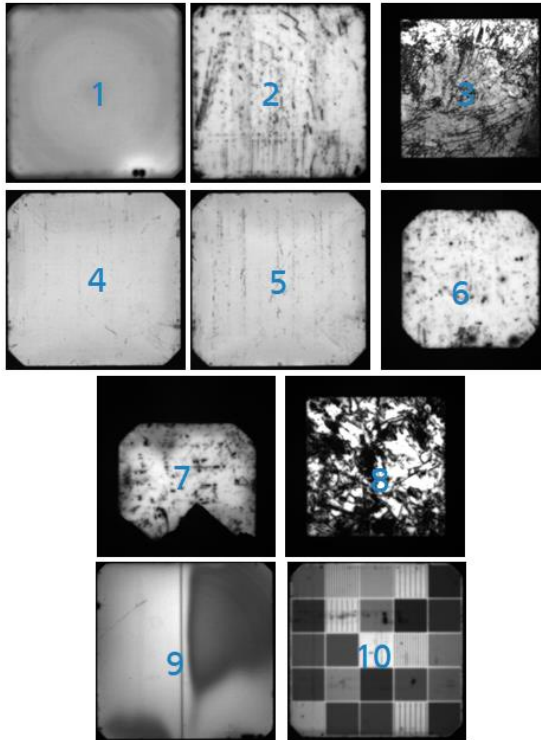
Figure 4: PL images of the wafers used for the validation experiment (scaled in arbitrary units, image size approx. 160 x 160 mm²).

Photoconductance decay measurements (often referred to as QSSPC) were conducted via a commercially available setup (WCT-120) on wafers 1-8. Mod-PL calibrated PLI measurements were conducted on one of our laboratory setups. The base doping, the thickness and the reflectance, which are necessary input parameters, were measured inductively, via capacitance and via an Ulbricht sphere respectively.

3.2 Reproducibility and consistency

Reproducibility: Reproducibility was checked on 3 wafers featuring different lifetime regimes (1, 4 and 6 from Figure 4). 10 consecutive Mod-PL measurements were carried out. The measured lifetimes at one specified minority carrier density (spec. MCD) are plotted in Figure 7. The deviation of a single measurement from the mean of the 10 consecutive measurements is plotted in Figure 8. As an illustrative example the Mod-PL raw data and the injection dependent lifetime of sample 1 is plotted in Figure 5 and Figure 6.
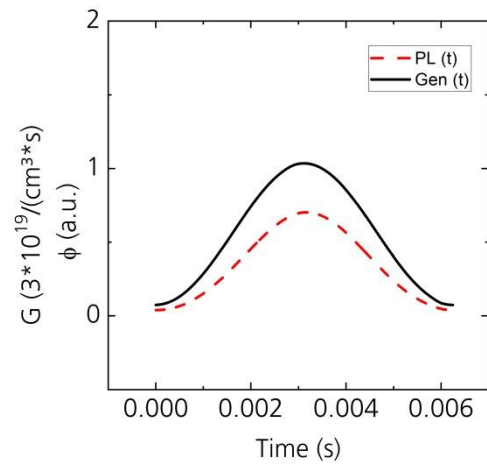
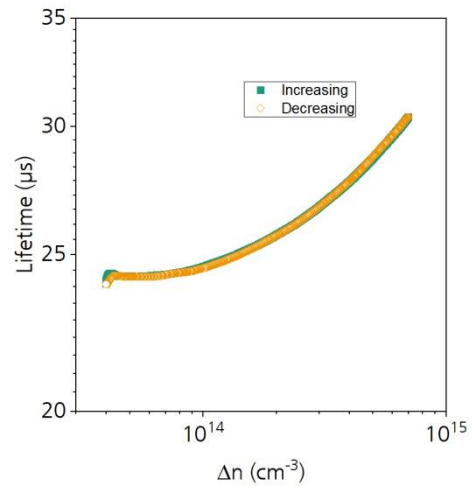Figure 5: Generation and luminescence signal of sample 1

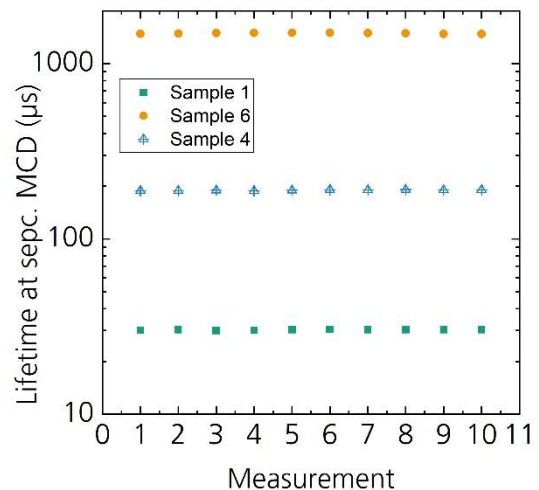Figure 6: Injection dependent lifetime of sample 1

Figure 7: Lifetime at a specified MCD of samples 1, 4 and 6 measured by 10 consecutive measurements; (d) deviation of each single value from the mean value of the 10 measurements
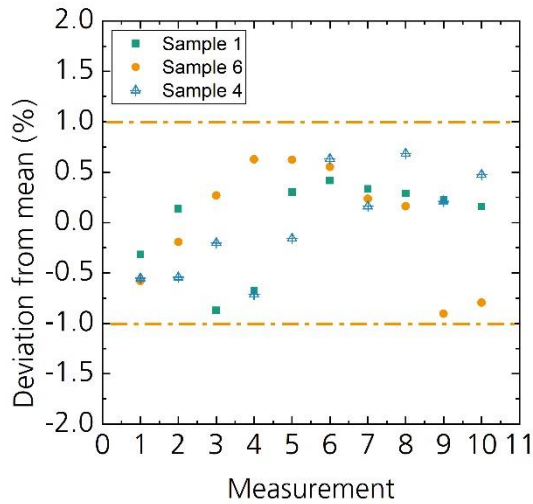
Figure 8: Deviation of each single value from the mean value of the 10 measurements

Consistency (frequency independence): In order to check whether the results are independent of the selected frequency during the Mod-PL measurement, samples 1, 4 and 6 were measured with different frequencies. The selected frequencies were varied around the automatically determined frequency (see section 2.1). Figure 9 shows lifetime results for consecutive Mod-PL measurements with different frequencies. Figure 10 shows the deviation of the single measurement with respect to the measurement with automatically determined frequency.
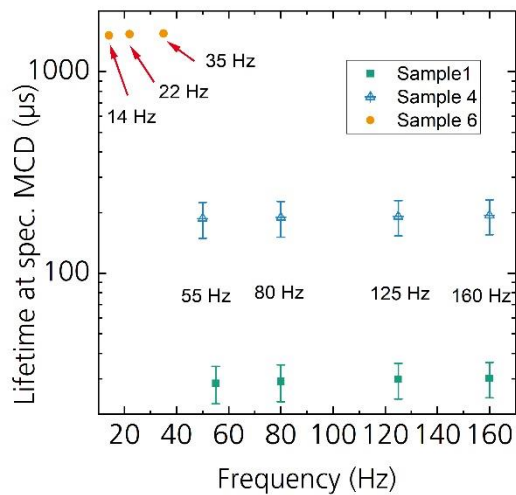
Figure 9: Lifetime at a specified MCD of sample 1, 4 and 6 measured with different frequencies. The error bars indicate a 10 % interval.
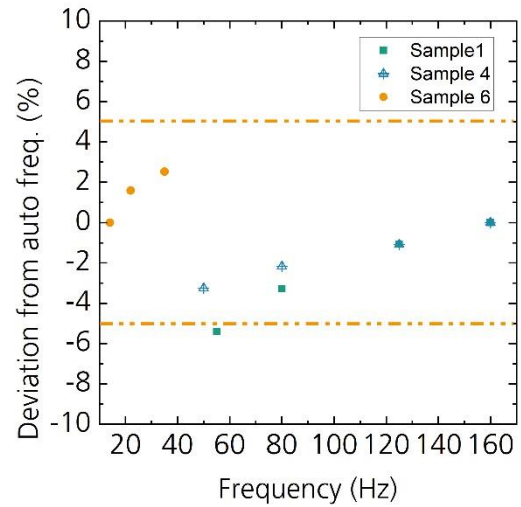

Figure 10: Deviation of the single measurements with respect to the lifetime measured with automatically detected frequency.

Consistency (independence of calibration position): A claim of the Mod-PL calibrated PLI method is that the lifetime images obtained by the method are independent of the calibration position. In order to check that, samples 4, 9 and 10 have been calibrated at different positions. While sample 4 represents a wafer with a rather homogeneous lifetime distribution, samples 9 and 10 intentionally represent wafers with an extremely inhomogeneous lifetime distribution. Figure 11 shows the lifetimes at a specified region of interest, that have been obtained by performing Mod-PL calibrated PLI at 9 different calibration positions. Figure 12 shows the deviation of the individual values from their mean value.
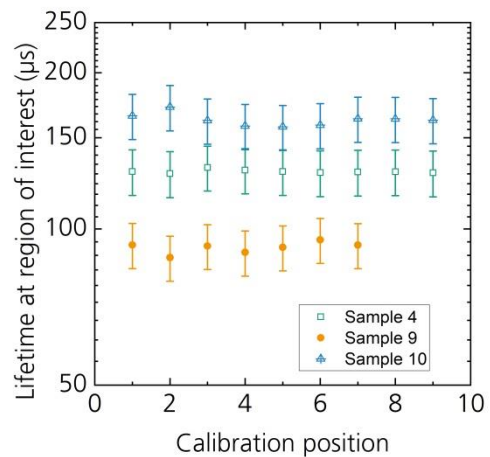

Figure 11: Lifetime of samples 4, 9 and 10 at a specified region of interest measured by Mod-PL calibrated PLI at different calibration positions (the error bars indicate a 10 % interval)
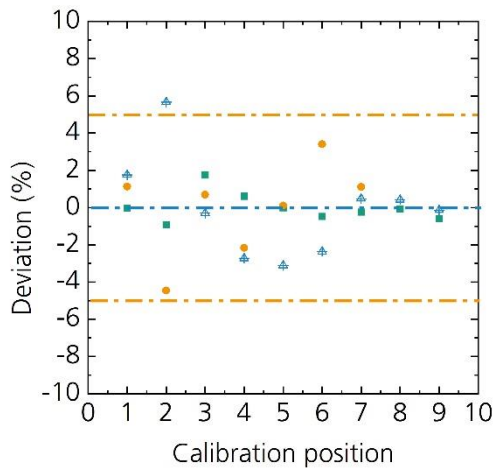
Figure 12: Deviation of the single values from their mean value

3.3 Comparison of Mod-PL calibrated PLI and QSSPC calibrated PLI

The samples 1-8 were measured with PLI, Mod-PLI and QSSPC. The PL images were calibrated with Mod-PL and with QSSPC. The lifetimes in the center of the obtained lifetime images are shown in Figure 14a). The deviation of the corresponding lifetime values from each other are shown in Figure 14 b).
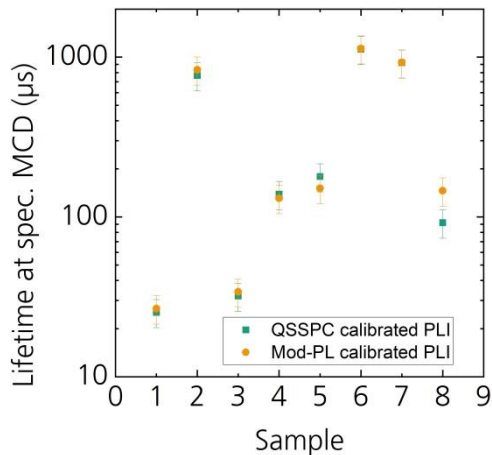

Figure 13: Lifetimes of sample 1-8 evaluated at the center of the lifetime images calibrated with Mod-PL and QSSPC respectively
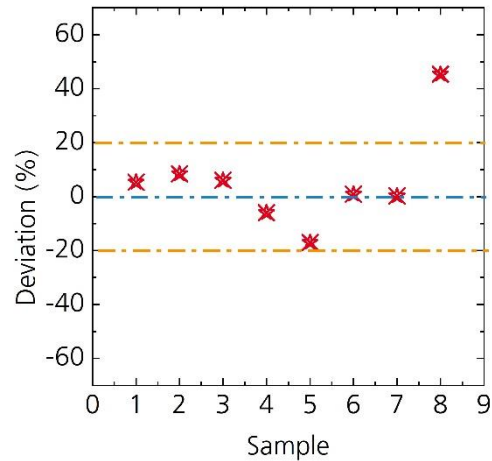

Figure 14: Deviation of the values from each other.

3.4 Discussion of results

As shown in Figure 8 the deviation of consecutive measurements are lower than one percent.

Figure 9 and Figure 10 show that the results slightly depend on the selected frequency. Ideally they should be completely independent of the selected frequency. Nevertheless the observed dependency is weak and the deviation with respect to the automatically determined frequency is below 5 %. Furthermore it is not expected that the results are completely independent of the modulation frequency. The cycle time has to be large compared to the sample lifetime. High modulation frequencies (short cycle times) may lead to a deviation of the quasi steady state condition if sample lifetimes are high. On the other hand low frequencies (high cycle time) will induce large measurement errors if sample lifetimes are low.

The results in Figure 11 and Figure 12 indicate that different calibration positions lead to deviation of less than 5 %. It should be noted that all possible artifacts of PLI (including camera vignette [49] and laser inhomogeneity [50]) and many possible artifacts of the Mod-PL measurements will lead to a dependence of the result from its calibration position. Combined with the fact that the wafers measured in this experiment were intentionally chosen to feature extreme lateral inhomogeneity the deviation of less than 5 % can be considered an excellent indication of the method's robustness.

Figure 14 shows that the deviation between the two measurement methods is smaller than 20 % (except for sample 8). In the first place it has to be mentioned that both methods (Mod-PL and QSSPC) may equally be subject to measurement uncertainties, so a deviation of a Mod-PL result from a QSSPC measurement does not necessarily need to be caused by artifacts originating from the Mod-PL measurement. An investigation by McIntosh *et al.* [51] concludes an error of around 5 to 10 % for the QSSPC measurements investigated in his work. Nevertheless the measurements undertaken in his work used a special calibration procedure for the WCT-120 instrument. The results of this work have been measured with the usual calibration procedure suggested by the manual of the commercially available instrument. Moreover it has recently been found, that the thickness differences between calibration wafers and sample wafers may cause a systematic error in the QSSPC measurements [52]. These facts could indicate that the uncertainty in the QSSPC measurements presented here is slightly larger than 10 %

and that the deviation is mainly caused by uncertainties of the QSSPC measurement. An uncertainty investigation of a measurement procedure, which is similar to the Mod-PL procedure described in this work can be found in [53]. Regarding these possible sources of uncertainty the agreement observed in Figure 14 can be considered to be very good. Sample 8 shows a large deviation. Large deviations between the measurement methods for multi crystalline wafers have already been observed by Giesecke (see [17] appendix C). There it is argued that the results are an indication (not a proof) for the fact that potential barriers at grain boundaries might lead to a misinterpretation of the results obtained by photoconductivity.

4 APPLICATION EXAMPLES FROM R&D

This section covers examples from our R&D environment, in which Mod-PL calibrated PLI is used.

4.1 Material analysis using ELBA

Mod-PL calibrated PLI allows to obtain a series of lifetime images at different illumination levels. It hence measures an injection dependent lifetime curve at each position of the wafer (image pixel). If these measurements are conducted on ideally passivated wafers it is possible to predict the efficiency potential of the investigated silicon material by an efficiency limiting bulk recombination analysis (ELBA) [42, 43]. In an ELBA the injection dependent bulk lifetime information is fed into a solar cell simulation model in order to predict the efficiency potential. The modulum evaluation software features a direct interface to the simulation environment Quokka 3 [54, 55], which allows an ELBA directly after the data acquisition. Schindler *et al.* [56] used an ELBA in order to predict the efficiency potential of different multi crystalline (mc) materials for TOPCon processing in 2017 (see Figure 15) . The selection of the material with the highest efficiency potential enabled by the ELBA allowed the fabrication of a 22.3 % mc-Solar cell [57], which represented a world record at the time.
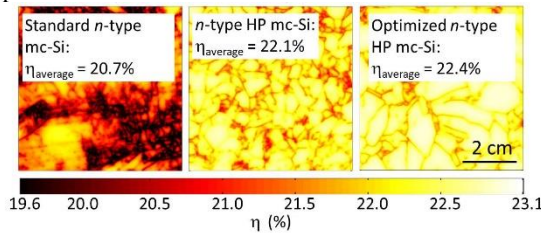

Figure 15: Visualization of ELBA results on 3 different mc-materials.

In a more recent study Schubert *et al.* [58] used ELBA to investigate the potential of seed manipulated (SMART) [59] material. An efficiency potential of 23.3 % is predicted by the ELBA and confirmed on the actual solar cells manufactured from the material.

4.2 Process optimization of laser doped selective emitter

Quantitative spatially resolved lifetime and iV_{oc} measurements are continuously used for process optimization in our R&D environment. The great benefit of the spatially resolved nature of the measurement is that a large number of process parameters can be realized on a single wafer. Figure 16 shows an example in which Mod-PL calibrated PLI is used for the optimization of a laser doped selective emitter (LDSE) [60] process. 49 test fields

are realized on one wafer with a passivated rear side and a phosphorous emitter plus phosphorous silicon glass (PSG) on the front. The emitter has been selectively doped using the PSG as a phosphorous source applying eight laser powers (a, b, …, f) and four different pitches (a, …, d). Each set of these 32 parameter variations has been applied to one test field. The test fields 1, 3, 5, 7, 15, 17, 19, 21, … are left unprocessed. A key idea of this test field geometry is that the unprocessed fields can serve as reference in order to correct for wafer inhomogeneity which is not process induced. A detailed presentation of the laser process optimization procedure using Mod-PL calibrated PLI involving a broad parameter variation and different laser processes will be published in a follow up paper.
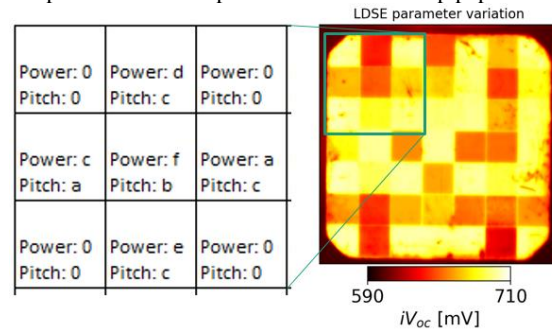

Figure 16: Visualization of process parameter optimization. The image on the right shows an iV_{oc} map of a wafer which was exposed to different LDSE parameters. In order to illustrate the key idea the parameters of the upper left nine fields are shown on the left.

Experiment designs like the one sketched in Figure 16 directly allow to attribute a voltage or a process induced voltage loss to a set of process parameters.

4.3 Metallization induced recombination losses

One benefit of lifetime measurements by Mod-PL over lifetime measurements by photoconductivity is that Mod-PL allows to measure metallized samples. This allows a very straight forward and simple approach to estimate the emitter saturation current density at the metallization $j_{0e,met}$ by realizing different metallization fractions on one wafer. Figure 17 shows an example layout of a wafer, which was metallized with different metallization fractions F on the rear side. The diode saturation current density $j_{0,xy}$ has been calculated via equation (8) and is shown in Figure 18. If a strongly simplified area weighted behavior (similar to the one proposed in [61]) is assumed one can write:

$$j_0 = j_{base,rear} + j_{0e,pass} + F\left(j_{0e,met} - j_{0e,pass}\right) \tag{11}$$

Plotting j_0 against F and evaluating the slope of the linear fit then directly reveals the term $(j_{0e,met} - j_{0e,pass})$. The example in Figure 19 reveals a slope of 1024 fA/cm². With $j_{0e,pass} = 60$ fA/cm² this corresponds to a $j_{0e,met}$ of roughly 1100 fA/cm².
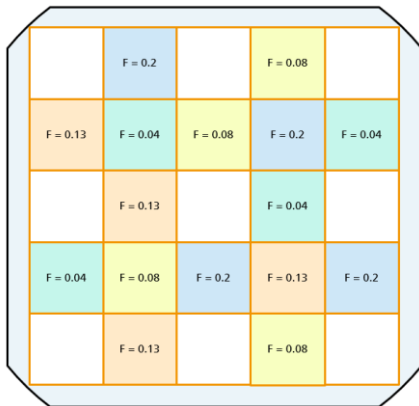
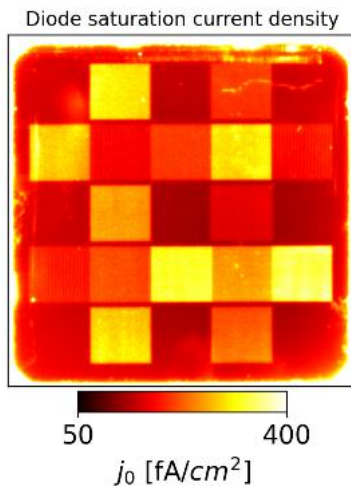Figure 17: Test field layout for the investigated sample.

Figure 18: Image of the diode saturation current density measured by Mod-PL calibrated PLI.
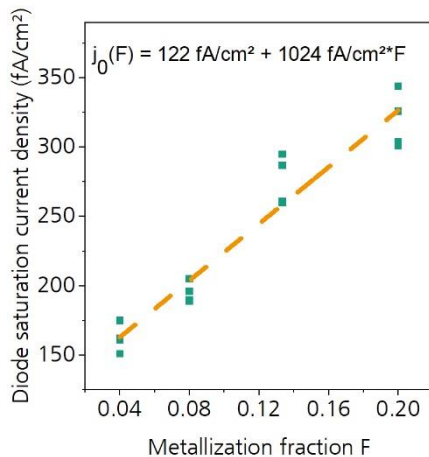

Figure 19: Sketch of simplified procedure for the determination of $j_{0e,met}$ by Mod-PL calibrated PLI. The diode saturation current density is plotted against the metallization fraction. The slope of a linear fit allows to determine $j_{0e,met}$.

It has to be pronounced that the above method makes some strongly simplifying assumptions. A much more sophisticated approach, which involves the simulation of the excess carrier distribution and a design of experiment where an interpolation scheme for the test field layout is applied, can be found in [62, 63]. In [63] a value of $j_{0e,met}$ of 1330 ± 190 fA/cm^2 has been determined for the same sample type. While the value of [63] is surely more precise, the method sketched above provides a very simple approach, which still reveals quantitative information with an accuracy, which is sufficient for many applications.

4.4 Cell analysis via C-DCR

The presence of a properly designed contacting unit and a source-sink, which allows to control the solar cell's working point in current and in voltage mode, enables the acquisition of the images that are needed for a C-DCR evaluation (see section 2.5). The spatially resolved nature of series resistance images calculated via the C-DCR approach are useful in order to differentiate quickly between fill factor losses that are caused by grid failures or those that are caused by an improper formation of the metal semiconductor contact. Figure 20 illustrates the benefit of the C-DCR evaluation. It shows images of the spatially resolved series resistance of two PERC solar cells. The cells have been equally processed apart from the fact that the right cell has been exposed to laser enhanced contact optimization (LECO) [64] after the firing step. Figure 20 (left) shows signatures, which can clearly be attributed to an improper metal semiconductor contact, and the cell features a fill factor of 20 %. The identification of the improper contact motivated the application of LECO to the other cells from that batch. Figure 20 (right) shows the series resistance obtained after the LECO process, and the cell features a fill factor of 78.5 %. Figure 20 (right) now allows to attribute the remaining fill factor losses to imperfections in the grid.
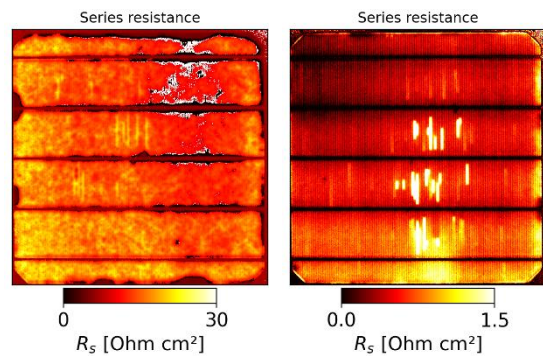

Figure 20: Series resistance image calculated by C-DCR of: (left) a PERC solar cell featuring grid failures and an improper metal semiconductor contact; (right) a PERC cell manufactured with the same processing but with an additional LECO step.

5   RECENT   DEVELOPMENT   USING TEMPERATURE CONTROLLED MEASUREMENTS

Mod-PL calibrated PL images can in principle be obtained at any wafer temperature if the measurement setup allows to control and measure the wafer temperature. The ability to control temperature has been used in recent works to obtain spatially resolved information about temperature coefficients and to allow defect classification and localization. The works will be sketched in the following.

5.1 Spatially resolved temperature coefficients

Eberle *et al.* recently used injection dependent lifetime images obtained by Mod-PL calibrated PLI at different temperatures to get spatially resolved information on temperature coefficients [65] and to predict the local temperature dependent performance of solar cells [66].

This is done by combining the temperature dependent measurements with an ELBA. A part of the necessary measurements are shown in Figure 21. Example results of the spatially resolved temperature coefficients adopted from [66] are shown in Figure 22. Via this approach, the physics behind local temperature sensitivities of the bulk can be studied e.g. showing decreased temperature sensitivity in low-quality areas of mc-Si, which might be caused by impurities and their SRH characteristics.
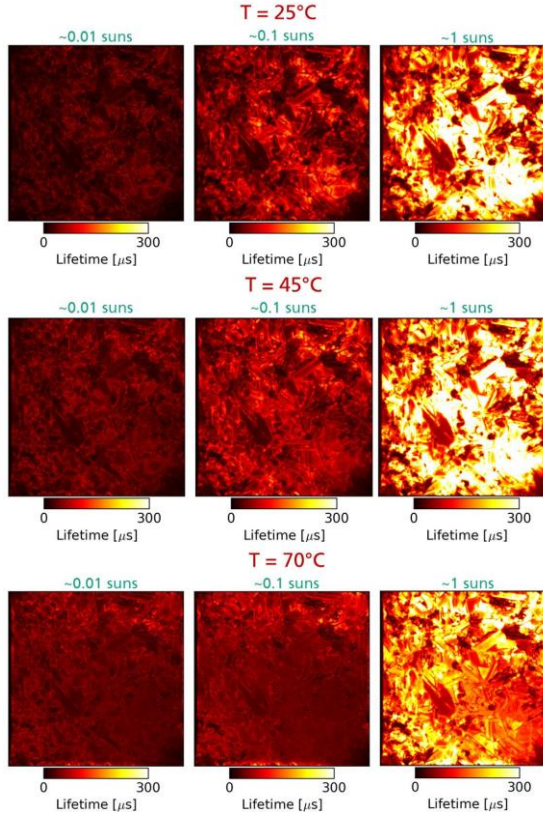

Figure 21: Injection and temperature dependent lifetime maps, which serve as the measurement data needed to obtain local temperature coefficients of the material.
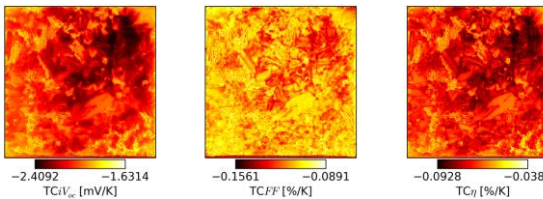

Figure 22: Images of the temperature coefficients of the material potential. (Details can be found in [66])

5.2 Defect classification and localization

Temperature and injection dependent PLI (TIDPLI) has recently been shown to be a powerful method for the classification and localization of defects [67, 68]. Figure 23 shows injection dependent lifetime curves evaluated from Mod-PL calibrated PLI images taken at temperatures up to 150°C. These curves directly allow the extraction of defect parameter solution surfaces (DPSS) [69]. The analysis of the DPSS intersection allows the determination of the defect parameters: capture cross sections ratio k and energy level E_t. A correspondence of these parameters with literature values allows spatially resolved defect classification. Details on this procedure will be given in an upcoming publication by Post *et al.*.
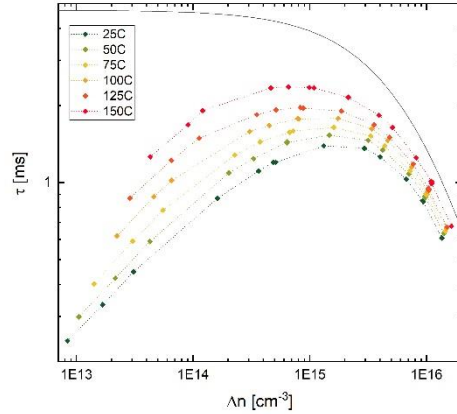

Figure 23: Injection dependent lifetime curves evaluated at different temperatures at one position of a multicrystalline wafer.

6   SUMMARY AND OUTLOOK

In this work we presented a canon of evaluation methods which is used for spatially resolved lifetime measurements via Mod-PL calibrated PLI. A measurement setup (modulum) providing the necessary hardware and featuring the canon of evaluation methods in its software has been developed over the past years. The setup allows to perform contacted ELI measurements and measurements at controlled temperatures between 15°C and 200°C. Lifetime measurements have been performed with the setup and have been checked for consistency and by a cross comparison to photoconductance based lifetime measurements. The tests revealed excellent reproducibility (<1 %) and a very robust behavior with respect to critical input parameters like frequency and calibration position (deviation < 5 %). Cross comparison to photoconductivity showed agreement within 10 % for most investigated samples. The deviations are partly attributed to the photoconductivity measurement.

An overview of the potential of temperature controlled spatially resolved lifetime measurements by Mod-PL calibrated PLI was given including the applications: efficiency prediction of silicon material, laser process optimization, quantitative determination of metal induced recombination, spatially resolved determination of series resistance, determination of material specific temperature coefficients and defect classification and localization by TIDPLI.

7   ACKNOWLEDGMENTS

References

[1]   W. Shockley and W. Read, "Statistics of the recombinations of holes and electrons," *Phys. Rev.*,

vol. 87, no. 5, pp. 835–842, 1952, doi: 10.1103/physrev.87.835.

[2] R. Hall, "Electron-hole recombination in germanium," *Phys. Rev.*, vol. 87, no. 2, p. 387, 1952, doi: 10.1103/PhysRev.87.387.

[3] D. K. Schroder, "Carrier lifetimes in silicon," *IEEE Trans. Electron Devices*, vol. 44, no. 1, pp. 160–170, 1997, doi: 10.1109/16.554806.

[4] R. A. Sinton, "Possibilities for process-control monitoring of electronic material properties during solar-cell manufacture," in *9th NREL Workshop on Crystalline Silicon Solar Cell Materials and Processes Golden*, Golden, CO, 1999, pp. 67–73.

[5] D. K. Schroder, *Semiconductor material and device characterization,* 3rd ed. Hoboken, New Jersey, USA: John Wiley & Sons, 2006.

[6] E. Yablonovitch and T. J. Gmitter, "A contactless minority lifetime probe of heterostructures, surfaces, interfaces and bulk wafers," *Solid-State Electronics*, vol. 35, no. 3, pp. 261–267, 1992, doi: 10.1016/0038-1101(92)90230-a.

[7] R. A. Sinton and A. Cuevas, "Contactless determination of current–voltage characteristics and minority-carrier lifetimes in semiconductors from quasi-steady-state photoconductance data," *Appl. Phys. Lett.*, vol. 69, no. 17, pp. 2510–2512, 1996, doi: 10.1063/1.117723.

[8] H. Nagel, C. Berge, and A. G. Aberle, "Generalized analysis of quasi-steady-state and quasi-transient measurements of carrier lifetimes in semiconductors," *J. Appl. Phys.*, vol. 86, no. 11, pp. 6218–6221, 1999, doi: 10.1063/1.371633.

[9] M. Kunst and G. Beck, "The study of charge carrier kinetics in semiconductors by microwave conductivity measurements," *J. Appl. Phys.*, vol. 60, no. 10, pp. 3558–3566, 1986, doi: 10.1063/1.337612.

[10] K. Dornich, "Elektrische Charakterisierung und Defektanalyse von Silizium mit MDP und MD-PICTS," PhD thesis, Technische Universität Bergakademie Freiberg, Freiberg, 2006.

[11] J. Dziewior and W. Schmid, "Auger coefficients for highly doped and highly excited silicon," *Applied Physics Letters*, vol. 31, no. 5, pp. 346–348, 1977, doi: 10.1063/1.89694.

[12] R. K. Ahrenkiel, "Measurement of minority-carrier lifetime by time-resolved photoluminescence," *Solid-State Electronics*, vol. 35, no. 3, pp. 239–250, 1992, doi: 10.1016/0038-1101(92)90228-5.

[13] S. Herlufsen *et al.,* "Dynamic photoluminescence lifetime imaging for the characterisation of silicon wafers," *Phys. Status Solidi RRL*, vol. 5, no. 1, pp. 25–27, 2011, doi: 10.1002/pssr.201004426.

[14] D. Kiliani, G. Micard, B. Steuer, B. Raabe, A. Herguth, and G. Hahn, "Minority charge carrier lifetime mapping of crystalline silicon wafers by time-resolved photoluminescence imaging," *Journal of Applied Physics*, vol. 110, no. 5, p. 54508, 2011, doi: 10.1063/1.3630031.

[15] J. A. Giesecke, M. C. Schubert, D. C. Walter, and W. Warta, "Minority carrier lifetime in silicon wafers from quasi-steady-state photoluminescence," *Appl. Phys. Lett.*, vol. 97, no. 9, p. 92109, 2010, doi: 10.1063/1.3485216.

[16] T. Trupke, R. A. Bardos, and M. D. Abbott, "Self-consistent calibration of photoluminescence and photoconductance lifetime measurements," *Appl.*

Phys. Lett., vol. 87, no. 18, p. 184102, 2005, doi: 10.1063/1.2119411.

[17] J. Giesecke, *Quantitative recombination and transport properties in silicon from dynamic luminescence*: Springer, 2014.

[18] G. Bohnert, R. Häcker, and A. Hangleiter, "Position resolved carrier lifetime measurements in silicon devices by time resolved photoluminescence," *J. Phys. Colloques*, vol. 49, C4, C4-617-C4-620, 1988, doi: 10.1051/jphyscol:19884128.

[19] W. Warta, J. Sutter, B. F. Wagner, and R. Schindler, "Impact of diffusion length distributions on the performance of mc-silicon solar cells," in *2nd World Conference on Photovoltaic Solar Energy Conversion Vienna*, Vienna, 1998, pp. 1650–1653.

[20] B. Berger, N. Schüler, S. Anger, B. Gründig-Wendrock, J. R. Niklas, and K. Dornich, "Contactless electrical defect characterization in semiconductors by microwave detected photo induced current transient spectroscopy (MD-PICTS) and microwave detected photoconductivity (MDP)," *Phys. Status Solidi A*, vol. 208, no. 4, pp. 769–776, 2011, doi: 10.1002/pssa.201083994.

[21] T. Trupke, R. A. Bardos, M. C. Schubert, and W. Warta, "Photoluminescence imaging of silicon wafers," *Appl. Phys. Lett.*, vol. 89, no. 4, p. 44107, 2006, doi: 10.1063/1.2234747.

[22] J. Isenberg, S. Riepe, S. W. Glunz, and W. Warta, "Imaging method for laterally resolved measurement of minority carrier densities and lifetimes: Measurement principle and first applications," *J. Appl. Phys.*, vol. 93, no. 7, pp. 4268–4275, 2003, doi: 10.1063/1.1555688.

[23] R. Brendel, M. Bail, B. Bodmann, J. Kentsch, and M. Schulz, "Analysis of photoexcited charge carrier density profiles in Si wafers by using an infrared camera," *Appl. Phys. Lett.*, vol. 80, no. 3, pp. 437–439, 2002, doi: 10.1063/1.1434308.

[24] S. Herlufsen, J. Schmidt, D. Hinken, K. Bothe, and R. Brendel, "Photoconductance-calibrated photoluminescence lifetime imaging of crystalline silicon," *Phys. Status Solidi RRL*, vol. 2, no. 6, pp. 245–247, 2008, doi: 10.1002/pssr.200802192.

[25] J. A. Giesecke, M. C. Schubert, B. Michl, F. Schindler, and W. Warta, "Minority carrier lifetime imaging of silicon wafers calibrated by quasi-steady-state photoluminescence," *Solar Energy Materials & Solar Cells*, vol. 95, pp. 1011–1018, 2011, doi: 10.1016/j.solmat.2010.12.016.

[26] T. Fuyuki, H. Kondo, T. Yamazaki, Y. Takahashi, and Y. Uraoka, "Photographic surveying of minority carrier diffusion length in polycrystalline silicon solar cells by electroluminescence," *Appl. Phys. Lett.*, vol. 86, no. 26, p. 262108, 2005, doi: 10.1063/1.1978979.

[27] T. Trupke, E. Pink, R. A. Bardos, and M. D. Abbott, "Spatially resolved series resistance of silicon solar cells obtained from luminescence imaging," *Applied Physics Letters*, vol. 90, no. 9, p. 93506, 2007, doi: 10.1063/1.2709630.

[28] K. Ramspeck, K. Bothe, D. Hinken, B. Fischer, J. Schmidt, and R. Brendel, "Recombination current and series resistance imaging of solar cells by combined luminescence and lock-in

thermography," *Appl. Phys. Lett.*, vol. 90, no. 15, p. 153502, 2007, doi: 10.1063/1.2721138.

[29] D. Hinken, K. Ramspeck, K. Bothe, B. Fischer, and R. Brendel, "Series resistance imaging of solar cells by voltage dependent electroluminescence," *Applied Physics Letters*, vol. 91, no. 18, p. 182104, 2007, doi: 10.1063/1.2804562.

[30] H. Kampwerth, T. Trupke, J. W. Weber, and Y. Augarten, "Advanced luminescence based effective series resistance imaging of silicon solar cells," *Applied Physics Letters*, vol. 93, no. 20, p. 202102, 2008, doi: 10.1063/1.2982588.

[31] M. Glatthaar, J. Haunschild, M. Kasemann, J. Giesecke, W. Warta, and S. Rein, "Spatially resolved determination of dark saturation current and series resistance of silicon solar cells," *Physica Status Solidi RRL*, vol. 4, no. 1, pp. 13–15, 2010, doi: 10.1002/pssr.200903290.

[32] H. Höffler, H. Al-Mohtaseb, J. Haunschild, B. Michl, and M. Kasemann, "Voltage calibration of luminescence images of silicon solar cells," *Journal of Applied Physics*, vol. 115, p. 34508, 2014, doi: 10.1063/1.4862400.

[33] H. Höffler, J. Haunschild, and S. Rein, "Influence of external contacting on electroluminescence and fill factor measurements," *Sol. Energy Mater. Sol. Cells*, vol. 152, pp. 180–186, 2016, doi: 10.1016/j.solmat.2016.03.039.

[34] H. Höffler, J. Haunschild, R. Zeidler, and S. Rein, "Statistical Evaluation of a Luminescence-Based Method for Imaging the Series Resistance of Solar Cells," *Energy Procedia*, vol. 27, pp. 253–258, 2012, doi: 10.1016/j.egypro.2012.07.060.

[35] M. Glatthaar *et al.,* "Evaluating luminescence based voltage images of silicon solar cells," *Journal of Applied Physics*, vol. 108, no. 1, p. 14501, 2010, doi: 10.1063/1.3443438.

[36] J. A. Giesecke, M. C. Schubert, and W. Warta, "Carrier Lifetime from Dynamic Electroluminescence," *IEEE J. Photovoltaics*, vol. 3, no. 3, pp. 1012–1015, 2013, doi: 10.1109/JPHOTOV.2013.2252236.

[37] P. Wurfel, "The chemical potential of radiation," *J. Phys. C: Solid State Phys.*, vol. 15, no. 18, pp. 3967–3985, 1982, doi: 10.1088/0022-3719/15/18/012.

[38] C. Schinke, D. Hinken, J. Schmidt, K. Bothe, and R. Brendel, "Modeling the Spectral Luminescence Emission of Silicon Solar Cells and Wafers," *IEEE J. Photovoltaics*, vol. 3, no. 3, pp. 1038–1052, 2013, doi: 10.1109/JPHOTOV.2013.2263985.

[39] P. P. Altermatt, F. Geelhaar, T. Trupke, X. Dai, A. Neisser, and E. Daub, "Injection dependence of spontaneous radiative recombination in crystalline silicon: Experimental verification and theoretical analysis," *Appl. Phys. Lett.*, vol. 88, no. 26, p. 261901, 2006, doi: 10.1063/1.2218041.

[40] S. P. Phang, H. C. Sio, and D. Macdonald, "Carrier de-smearing of photoluminescence images on silicon wafers using the continuity equation," *Applied Physics Letters*, vol. 103, no. 19, p. 192112, 2013, doi: 10.1063/1.4829658.

[41] A. Schenk, "Finite-temperature full random-phase approximation model of band gap narrowing for silicon device simulation," *J. Appl. Phys.*, vol. 84, no. 7, p. 3684, 1998, doi: 10.1063/1.368545.

[42] B. Michl, M. Rüdiger, J. A. Giesecke, M. Hermle, W. Warta, and M. C. Schubert, "Efficiency limiting bulk recombination in multicrystalline silicon solar cells," *Solar Energy Materials & Solar Cells*, vol. 98, pp. 441–447, 2012, doi: 10.1016/j.solmat.2011.11.047.

[43] B. Michl, M. Kasemann, W. Warta, and M. C. Schubert, "Wafer thickness optimization for silicon solar cells of heterogeneous material quality," *Phys. Status Solidi RRL*, vol. 7, no. 11, pp. 955–958, 2013, doi: 10.1002/pssr.201308090.

[44] B. Michl, D. Impera, M. Bivour, W. Warta, and M. C. Schubert, "Suns-PLI as a powerful tool for spatially resolved fill factor analysis of solar cells," *Prog. Photovolt: Res. Appl.*, vol. 22, no. 5, pp. 581–586, 2014, doi: 10.1002/pip.2293.

[45] Z. Hameiri and P. Chaturvedi, "Spatially resolved electrical parameters of silicon wafers and solar cells by contactless photoluminescence imaging," *Applied Physics Letters*, vol. 102, no. 073502, 2013, doi: 10.1063/1.4792348.

[46] H. Höffler, "Lumineszenz-Imaging Anwendungen in industrieller Fertigungsumgebung von Silicium-Solarzellen," PhD thesis, University of Freiburg, Freiburg, 2015.

[47] D. Hinken, C. Schinke, S. Herlufsen, A. Schmidt, K. Bothe, and R. Brendel, "Experimental setup for camera-based measurements of electrically and optically stimulated luminescence of silicon solar cells and wafers," *Rev. Sci. Instrum.*, vol. 82, no. 3, p. 33706, 2011, doi: 10.1063/1.3541766.

[48] F. Simon, "Optimierung und Evaluation der elektrischen Kontaktierung des Photo- und Elektrolumineszenz-Messstandes modulum," Bachelor thesis, TH Köln - University of applied science, Köln, 2019.

[49] G. Dost, H. Höffler, and J. M. Greulich, "Vignetting in luminescence imaging of solar cells," *Review of Scientific Instruments*, vol. 90, no. 10, p. 103707, 2019, doi: 10.1063/1.5125101.

[50] H. Höffler, G. Dost, A. Brand, J. Haunschild, H. Schremmer, and A. Bergmann, "Comparison of line-wise pl-imaging and area-wise pl-imaging," *Energy Procedia*, vol. 124, pp. 66–75, 2017, doi: 10.1016/j.egypro.2017.09.341.

[51] K. R. McIntosh, R. A. Sinton, and K. R. McIntosh, "Uncertainty in Photoconductance Lifetime Measurements that Use an Inductive-Coil Detector," in *23rd EU PVSEC*, Valencia, 2008, pp. 77–82.

[52] L. E. Black and D. H. Macdonald, "Accounting for the Dependence of Coil Sensitivity on Sample Thickness and Lift-Off in Inductively Coupled Photoconductance Measurements," *IEEE J. Photovoltaics*, vol. 9, no. 6, pp. 1563–1574, 2019, doi: 10.1109/JPHOTOV.2019.2942484.

[53] Z. Hameiri, K. R. McIntosh, T. Trupke, Z. Hameiri, and T. Trupke, "Uncertainty in Photoluminescence-Based Effective Carrier Lifetime Measurements," in *38th IEEE Photovoltaic Specialists Conference Austin*, Austin, Texas, 2012, pp. 390–395.

[54] A. Fell, *quokka3.* [Online]. Available: www.quokka3.com (accessed: Jan. 22 2018).

[55] A. Fell, "A free and fast three-dimensional/two-dimensional solar cell simulator featuring conductive boundary and quasi-neutrality

approximations," *IEEE Trans. Electron Devices*, vol. 60, no. 2, pp. 733–738, 2013, doi: 10.1109/TED.2012.2231415.

[56] F. Schindler *et al.,* "Optimized multicrystalline silicon for solar cells enabling conversion efficiencies of 22%," *Sol. Energy Mater. Sol. Cells*, vol. 171, pp. 180–186, 2017, doi: 10.1016/j.solmat.2017.06.005.

[57] F. Schindler *et al.,* "Towards the efficiency limits of multicrystalline silicon solar cells," *Sol. Energy Mater. Sol. Cells*, vol. 185, pp. 198–204, 2018, doi: 10.1016/j.solmat.2018.05.006.

[58] M. C. Schubert *et al.,* "The Potential of Cast Silicon," *to be published*, 2020.

[59] I. Takahashi, S. Joonwichien, T. Iwata, and N. Usami, "Seed manipulation for artificially controlled defect technique in new growth method for quasi-monocrystalline Si ingot based on casting," *Appl. Phys. Express*, vol. 8, no. 10, p. 105501, 2015, doi: 10.7567/APEX.8.105501.

[60] L. Ventura, A. Slaoui, and J. C. Muller, "Realization of selective emitters by rapid thermal and laser assisted techniques," in *13th EU PVSEC*, Nice, 1995, pp. 1578–1581.

[61] T. Fellmeth, A. Born, A. Kimmerle, F. Clement, D. Biro, and R. Preu, "Recombination at metal-emitter interfaces of front contact technologies for highly efficient silicon solar cells," *Energy Procedia*, vol. 8, pp. 115–121, 2011, doi: 10.1016/j.egypro.2011.06.111.

[62] D. Herrmann, S. Lohmuller, H. Hoffler, A. Fell, A. A. Brand, and A. Wolf, "Numerical Simulations of Photoluminescence for the Precise Determination of Emitter Contact Recombination Parameters," *IEEE J. Photovoltaics*, vol. 9, no. 6, pp. 1759–1767, 2019, doi: 10.1109/JPHOTOV.2019.2938400.

[63] D. Herrmann *et al.,* "Spatially Resolved Determination of Metallization-Induced Recombination Losses Using Photoluminescence Imaging," *IEEE Journal of photovoltaics*, to be published, 2020.

[64] R. Mayberry, K. Myers, V. Chandrasekaran, A. Henning, H. Zhao, and E. Hofmüller, "Laser Enhanced Contact Optimization (LECO) and LECO-Specific Pastes - A Novel Technology for Improved Cess Efficiency," *36th European Photovoltaic Solar Energy Conference and Exhibition*, 2019.

[65] R. Eberle, S. T. Haag, I. Geisemeyer, M. Padilla, and M. C. Schubert, "Temperature Coefficient Imaging for Silicon Solar Cells," *IEEE J. Photovoltaics*, vol. 8, no. 4, pp. 930–936, 2018, doi: 10.1109/JPHOTOV.2018.2828839.

[66] R. Eberle, A. Fell, S. Mägdefessel, F. Schindler, and M. C. Schubert, "Prediction of local temperature-dependent performance of silicon solar cells," *Progress in Photovoltaics: Research and Applications*, vol. 27, no. 11, pp. 999–1006, 2019, doi: 10.1002/pip.3130.

[67] L. E. Mundt *et al.,* "Spatially resolved impurity identification via temperature- and injection-dependent photoluminescence imaging," *IEEE J. Photovoltaics*, vol. 5, no. 5, pp. 1503–1509, 2015, doi: 10.1109/JPHOTOV.2015.2447837.

[68] J. Schön *et al.,* "Identification of lifetime limiting defects by temperature- and injection-dependent photoluminescence imaging," *J. Appl. Phys.*, vol. 120, no. 10, p. 105703, 2016, doi: 10.1063/1.4961465.

[69] S. Rein, T. Rehrl, W. Warta, and S. W. Glunz, "Lifetime spectroscopy for defect characterization:: Systematic analysis of the possibilities and restrictions," *J. Appl. Phys.*, vol. 91, no. 4, pp. 2059–2070, 2002, doi: 10.1063/1.1428095.